crystals

MDPI

Review

Cerium-Doped Oxide-Based Materials for Energy and Environmental Applications

Suhwan Kim [1], Minho Choi [2] and Jongsung Park [2,*]

[1] Future Convergence Technology Research Institute, Gyeongsang National University, Jinju 52828, Gyeongnam, Republic of Korea; sh-kim@gnu.ac.kr
[2] Department of Energy Engineering, Gyeongsang National University, Jinju 52828, Gyeongnam, Republic of Korea
* Correspondence: j.park@gnu.ac.kr

Abstract: Cerium is a rare-earth metal commonly used as a dopant in various metal oxides to enhance their performances or provide optoelectronic properties. Cerium oxide (ceria) is particularly valuable owing to its unique properties and applications in various fields, such as biomedical research, photovoltaics, and industrial catalytic processes. This review focuses on the use of cerium and ceria doping in the synthesis of SiO_2 and ZnO. Studies have shown that Ce-doped SiO_2 thin films exhibit luminescence properties and proton shielding capabilities, and that Ce-doped ZnO has potential applications in gas sensors. In this review, we highlight the potential for controlling the luminescence and optical characteristics of these materials via cerium doping, opening up possibilities for various technological advancements and potential applications of cosmic ray shielding in space photovoltaics.

Keywords: cerium doping; Ce-doped glass; Ce-doped ZnO; space solar cell

check for updates

Citation: Kim, S.; Choi, M.; Park, J. Cerium-Doped Oxide-Based Materials for Energy and Environmental Applications. *Crystals* **2023**, *13*, 1631. https://doi.org/10.3390/cryst13121631

Academic Editors: Lin Gan and Rajratan Basu

Received: 10 October 2023
Revised: 12 November 2023
Accepted: 21 November 2023
Published: 24 November 2023

Copyright: © 2023 by the authors. Licensee MDPI, Basel, Switzerland. This article is an open access article distributed under the terms and conditions of the Creative Commons Attribution (CC BY) license (https://creativecommons.org/licenses/by/4.0/).

1. Introduction

Cerium is the most abundant rare-earth metal in the Earth's crust. Cerium minerals include carbonates, phosphates, silicates, and hydroxides. Cerium is the first element in the periodic table to have orbitals partially filled with f and d ($[Xe]4f^15d^16s^2$) [1]. As a lanthanide, it has two stable oxidation states: Ce^{3+} and Ce^{4+}. The latter state has a noble gas structure with an atomic radius of 0.90 Å [2]. Owing to their superior redox characteristics and oxygen storage capacity in stable Ce^{3+} and Ce^{4+} oxide states, cerium ions have long been utilized as well-studied dopants in catalytic systems [3,4]. The Ce^{4+}/Ce^{3+} redox property effectively improves the separation of electron–hole pairs in the photocatalyst system [5,6]. In addition, the 4f levels of cerium are shielded by Ce^{3+}, resulting in well-defined, narrow optical transitions between spin–orbit levels. Cerium strongly absorbs and emits within the visible range of ultraviolet–visible light (UV-Vis) and photoluminescence (PL) spectra.

Cerium oxide (ceria) holds significant technological value owing to its distinctive properties. Ce exists in two oxidation states: Ce^{3+} and Ce^{4+}. Consequently, ceria exists in two forms in bulk materials: CeO_2 (with Ce^{4+}) and Ce_2O_3 (with Ce^{3+}). The Ce oxide lattice has a nanoscale cubic fluorite structure, and Ce^{3+} and Ce^{4+} can coexist on its surface. Oxygen vacancies in the lattice compensate for the charge deficit owing to the presence of Ce^{3+}. Therefore, Ce oxide contains intrinsic oxygen defects [7]. These oxygen defects are the most decisive reason ceria is an important dopant. Numerous studies have focused on the wide range of applications of ceria-based structures. They are important in biomedical research [8–11], photovoltaics [12–14], ionic conductivity [15–17], solid oxide fuel cells [18–20], industrial catalytic processes [21], automotive catalysts [22], and soot oxidation catalysts [23–25].

In this review, we focus on cerium-doped metal oxide, particularly SiO_2 and ZnO. We introduce studies on the luminescence properties, improvement in chemical durability,

solar cell characteristics of Ce-doped SiO_2, and its proton-shielding properties in aerospace applications, which have not been extensively studied in other reviews. We also discuss studies on the physical properties of Ce-doped ZnO, a group II-V semiconductor, and its applications in UV photodetectors, reusable water treatment materials, and gas sensors. In addition, we provide insights into the potential use of Ce-doped metal oxide as a galactic cosmic ray (GCR) protection layer in space photovoltaic applications.

2. Ce-Doped SiO_2

Ce-containing or -doped glasses have been studied mainly for UV or X-ray shielding, radiation measurements, and the prevention of darkening effects caused by GCR radiation [26,27]. When Ce is incorporated into the SiO_2 system, a new localized impurity band appears between the valence band maximum (VBM) and the conduction band minimum (CBM) of the SiO_2 system, which is primarily induced by the Ce-4f orbitals. The new localized impurity band that forms after Ce incorporation into SiO_2 is significant because it forms a bridge between the valence and conduction bands, making electronic transitions much more accessible. The Ce-doped SiO_2 system has a lower bandgap energy and a higher absorption coefficient than those of the pure SiO_2 system, which makes it a promising material for optoelectronic applications such as photovoltaic devices, light-emitting diodes, and photocatalysts [28].

J.S. Stroud (1961) measured the changes in the light absorption of Ce-containing glasses and electron spin resonance spectra when exposed to near-UV light [29]. The study showed that Ce^{3+} in SiO_2 was photoionized to Ce^{4+} under UV irradiation using samples of 75% SiO_2, 25% Na_2O, and 0.06% cerium oxide, which were melted under various reducing and oxidizing conditions. G.A. Haynes (1970) first reported that Ce-doped cover glass can improve radiation resistance performance. Synthetic fused quartz, which has been used as a radiation-resistant material, is prone to breakage when made thin, and sapphire is expensive [30]. This result shows that the cover glass doped with cerium oxide can perform similarly to the synthetic fused quartz. When the cover glass was doped with 1–2 wt% Ce, the radiation resistance performance improved for electron radiation in the range of ~1 MeV and proton radiation in the range of ~22 MeV. Based on the initial results of these UV-responsive and radiation-resistant properties, further research on their application in specific fields was conducted.

While bulk Si does not emit light, Si nanocrystals in silicon-rich silicon oxide films exhibit luminescence in the visible-near-infrared range, and the optical properties of these films can be further tuned via doping with optically active lanthanide atoms. Among them, Ce^{3+} ions have drawn interest because they are expected to luminesce in the ultraviolet blue range, making Ce-based materials useful for various applications. Weimmerskirch-Aubatin and Jennifer et al. (2015) investigated the optical properties of Ce-doped SiO_2 thin films, specifically their luminescence behavior with respect to the Ce content and annealing temperature [31]. Ce-doped thin films were prepared by co-evaporating Ce from a Knudsen cell heated to 1400 °C in an ultra-high vacuum chamber and SiO_2 powder from an electron beam gun at room temperature (RT). The concentration of Ce, defined as [Ce]/([Si] + [O] + [Ce]), was varied from 1 to 6% and the thickness was controlled at 200 nm using a quartz microbalance. The detection of significant blue luminescence at RT from the as-deposited films suggests that these materials have the potential for efficient light emission. At 1100 °C, developing a cerium silicate phase opens up the possibility of synthesizing novel Ce-based materials with customized optical characteristics (Figure 1). These findings imply that the luminescence of the films can be controlled by altering the Ce content and annealing temperature, enabling the creation of blue light-emitting diodes compatible with Si technology.

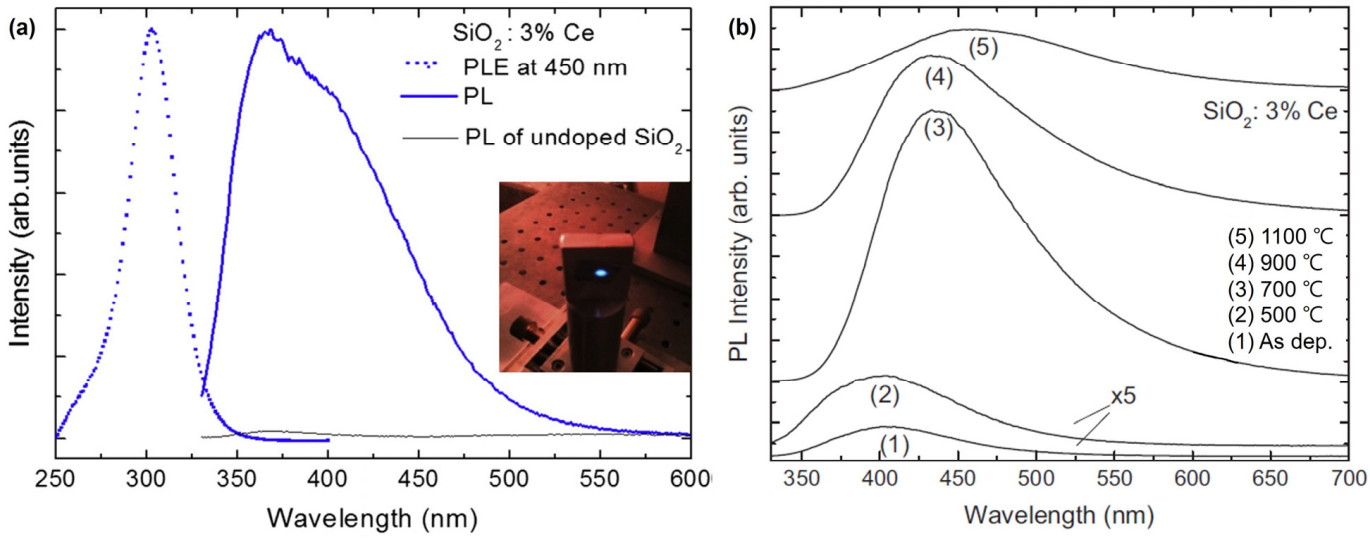

Figure 1. (**a**) Room-temperature steady-state PL spectrum (blue solid line) from an as-deposited 3% Ce-doped SiO_2 film excited at 325 nm and the corresponding PL excitation (PLE) spectrum (blue dotted line) measured at 450 nm. (**b**) Evolution of the PL spectra of the 3% Ce-doped SiO_2 film as a function of the annealing temperature (adapted with permission from Ref. [31]. Copyright 2014 Elsevier).

In addition to enabling wavelength tuning, Ce doping also improves luminescence characteristics. M. L. Su et al. (2022) investigated the enhanced luminescence characteristics achieved via the Ce doping of a $CsPbBr_3$ precursor and nanocrystal glass [32]. $CsPbBr_3$ has high quantum efficiency and color-tunable radioluminescence. However, their environmental stabilities remain unclear. Glass ceramics embedded with nanocrystals possess excellent luminescent properties and good mechanical and chemical stability related to the glass matrix [33]. Additionally, in borosilicate glass, the Ce^{3+} ion exhibits efficient blue emission (~420 nm), matching the excitation spectrum of $CsPbBr_3$ nanocrystals [34]. Incorporating Ce^{3+} ions into the glass matrix effectively transfers the X-rays absorbed by the glass to the $CsPbBr_3$ nanocrystals, thereby enhancing the luminescence intensity.

To begin, SiO_2, B_2O_3, CaO, Li_2CO_3, Sb_2O_3, $PbBr_2$, CsBr, and CeO_2 were mixed in a crucible and melted at 1200 °C for 15 min. The glass melt was placed in a warmed copper mold at 350 °C, annealed at 400 °C for six hours, and then cooled down to RT to reduce the thermal tension inside the precursor glass (PG). Subsequently, the samples were heat-treated at 550 °C for different durations, indicated as $CsPbBr_3$ nanocrystals–glass ($CsPbBr_3$ NG). Differential thermal analysis (DTA), X-ray diffraction (XRD), UV/VIS/NIR spectrophotometry, PL spectroscopy, and quantum efficiency measurements were performed.

They incorporated Ce^{3+} ions into the borosilicate glass matrix and enhanced green emission under 365 nm UV and X-ray irradiation. The luminous quantum efficiency reached up to 28% after heat treatment at 550 °C for 12 h. The X-ray-stimulated luminescence intensity of Ce^{3+}-doped $CsPbBr_3$ nanocrystals-glass was approximately 190% greater than that of undoped $CsPbBr_3$ nanocrystals–glass, showing the effective absorption of ray energy by Ce^{3+} ions. Following heat treatment, $CsPbBr_3$ nanocrystals precipitated from the glass matrix, resulting in high light absorption below 475 nm. The transparency of the $CsPbBr_3$ nanocrystals–glass decreased marginally with an increasing heat treatment time owing to the progressive development of nanocrystals. The $CsPbBr_3$ NG 550-12 h sample demonstrated high luminous intensity and reasonably high transmittance (80% at 527 nm) in the emission range. The photoluminescence peaks of the $CsPbBr_3$ nanocrystals changed from 490 to 527 nm as the heat treatment duration increased, indicating a quantum size impact. The PL and XEL intensities of Ce^{3+}-doped $CsPbBr_3$ NG 550-12 h were enhanced by 1.4 and 1.9 times, respectively, compared to those of the undoped $CsPbBr_3$ NG (Figure 2).

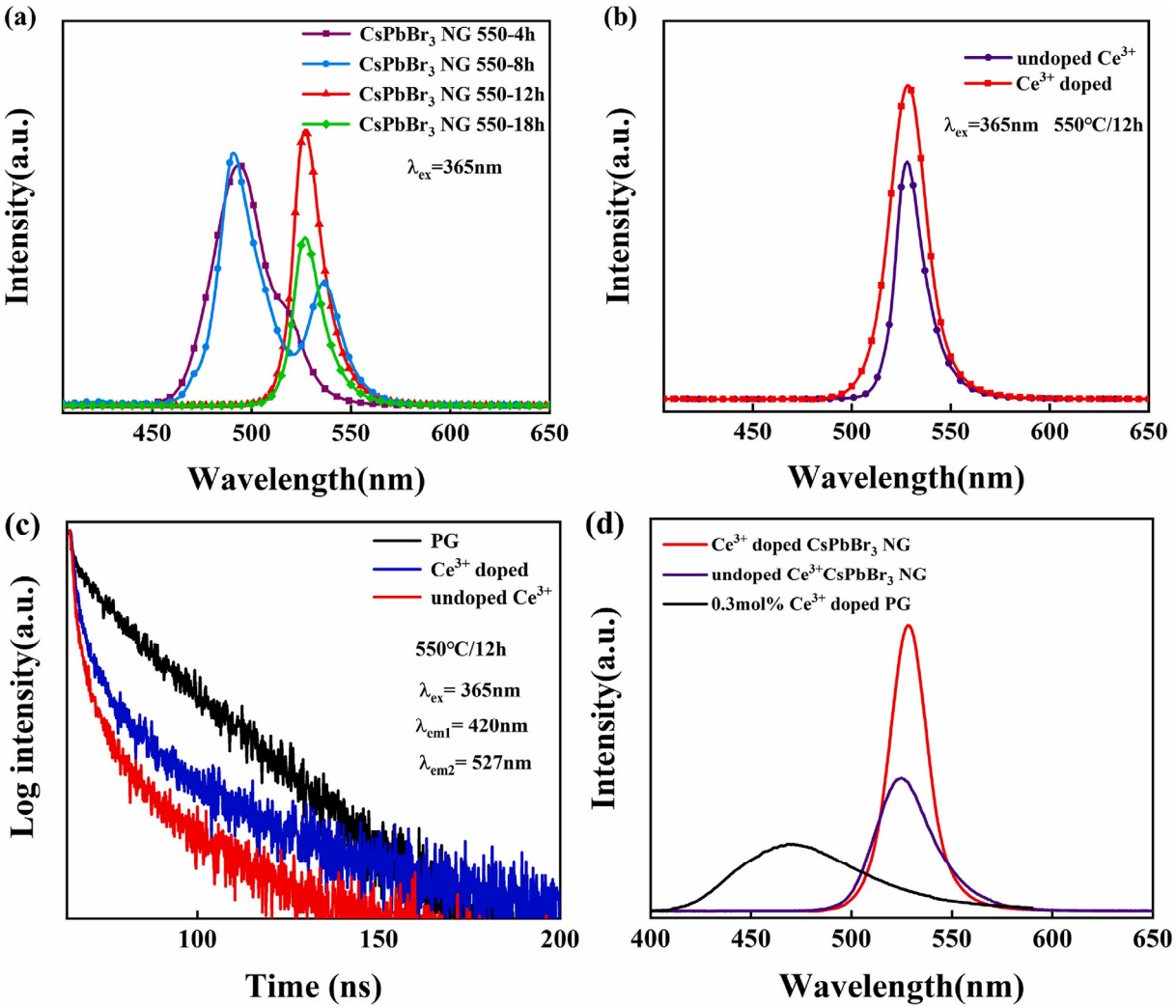

Figure 2. PL spectra under 365 nm excitation. (**a**) $CsPbBr_3$ NG in different heat treatment times; (**b**) undoped Ce^{3+} $CsPbBr_3$ NG and 0.3 mol% Ce^{3+}-doped $CsPbBr_3$ NG. (**c**) Fluorescence decay curves of three different samples under the excitation of 365 nm; (**d**) XEL spectra of 0.3 mol Ce^{3+}-doped PG, undoped, and Ce^{3+}-doped $CsPbBr_3$ NG 550-12 h samples (adapted with permission from Ref. [32]. Copyright 2021 Elsevier).

The $CsPbBr_3$ nanocrystal–glass composite scintillators demonstrate vigorous luminescent intensity and moderately high transmittance, making them appropriate for scintillator-based indirect-type X-ray detectors; the introduction of Ce^{3+} ions into the borosilicate glass matrix enhanced the green emission and higher X-ray-stimulated luminescence intensity in $CsPbBr_3$ nanocrystal–glass composite scintillators. The generated $CsPbBr_3$ nanocrystal scintillators based on Ce^{3+}-doped borosilicate glass are considered viable candidates for scintillator-based indirect-type X-ray detectors owing to their low cost, low detection limit, color-tunable emission, and fast decay characteristics.

Optical or thermally stimulated luminescence has been reported in Ce-doped glass rather than the steady-state luminescence mentioned above. G. Okada et al. (2016) reported that Ce-doped SiO_2 glass exhibited optically stimulated luminescence (OSL) and thermally stimulated luminescence (TSL) [35]. Ce-doped SiO_2 glass was prepared using spark plasma sintering, a solid-state reaction technique, instead of conventional methods such as sol–gel synthesis. SiO_2 (99.9% purity) glass nano-sized powder and CeO_2 (99.99% purity) powder were mixed in a weight ratio of 100:1. The mixture was then loaded into a graphite die and sealed with graphite punches. Subsequently, the assembly was sintered in a furnace under vacuum, with a temperature increase from 600 °C to 1300 °C at a rate of 10 °C/min and a

pressure of 70 MPa. The prepared samples were characterized using various techniques. The PL spectrum was measured using 265 nm excitation light, and the X-ray-induced luminescence (XL) spectrum was measured using an X-ray tube. The optically stimulated luminescence (OSL) emission spectrum was measured via stimulation using a 630 nm LED, and the thermally stimulated luminescence (TSL) glow curve was measured using a reader (Figure 3). The linear relationship between the OSL and TSL intensities and the incident radiation dose over the range of 1 mGy to 2 Gy indicates the potential for accurate dose measurement. Thus, Ce-doped glass is a good radiophotoluminescent (RPL) material for practical applications.

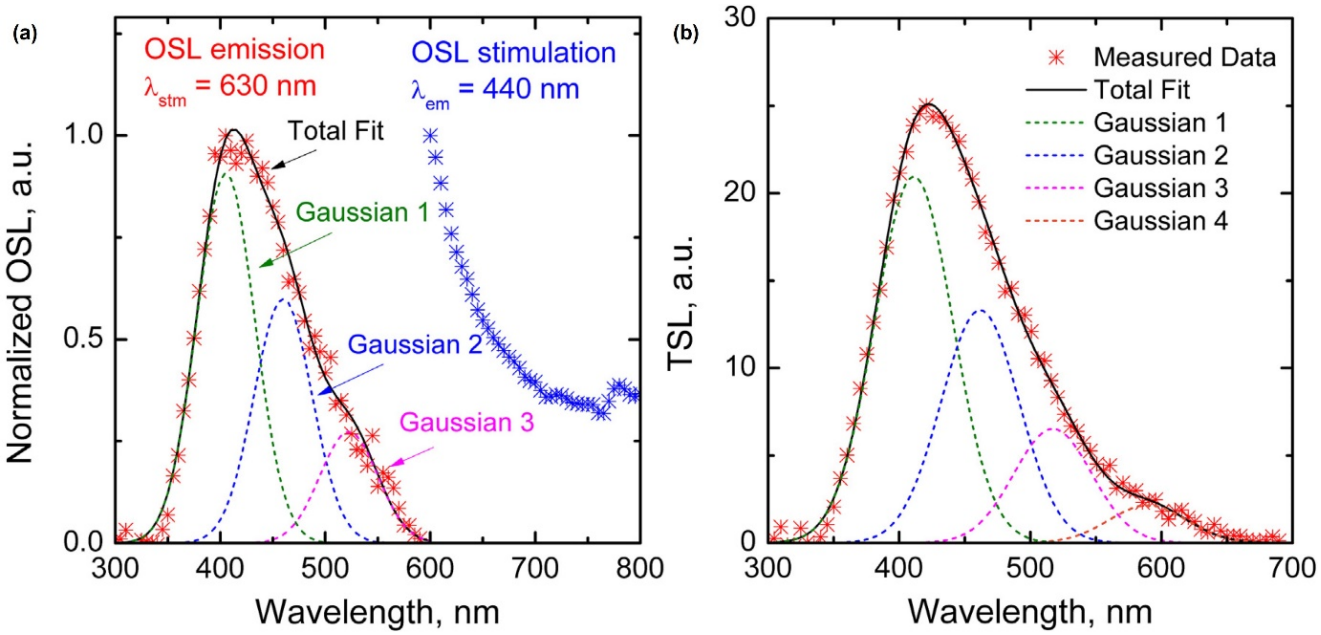

Figure 3. (**a**) Normalized OSL emission and stimulation spectra of SiO_2:Ce^{3+} glass and (**b**) TSL spectrum recorded at 250 °C (adapted with permission from Ref. [35]. Copyright 2016 Elsevier).

Cerium oxide has also drawn interest owing to its potential therapeutic applications. Its close electronegativity and ionic radii make it a suitable replacement for calcium in bioactive systems. Ce^{3+} ions possess antimicrobial properties and low toxicity [36,37]. They are recognized for their ability to produce collagen, which increases the mechanical strength and elasticity of skin [38].

P. Kaur et al. (2020) showed that the addition of cerium oxide (CeO_2) to bioceramic samples affected their bioactivity, degradation rate, cell survival response, and antioxidant characteristics [39]. The bioceramic samples were created via a sol–gel technique, employing $Si(OC_2H_5)_4$ and $(C_2H_5)_3PO_4$ precursors and alkaline earth metal sources, including $Ca(NO_3)_2{\cdot}4H_2O$, $Mg(NO_3)_2{\cdot}6H_2O$, and $Ce(NO_3)_3{\cdot}6H_2O$. The acid–catalyst sol–gel technique involves six phases and utilizes nitric acid as a hydrolysis catalyst. The samples were kept, aged, calcined, and described using agar and mortar. The Ce-doped $CaO–P_2O_5–MgO–SiO_2$ bioceramic samples were subsequently crushed for fine powder manufacture.

XRD analysis was performed to obtain XRD patterns and compare them with standard data files. Raman spectroscopy was used to examine the vibrational modes before and after in vitro analysis. Zeta potential experiments were performed to measure the fluctuations in zeta potential before and after in vitro analysis.

Samples with higher cerium concentrations exhibited a decrease in the growth rate of hydroxyapatite (HA) and the synthesis of cerium phosphate instead of HA on their surfaces. Despite the decrease in the HA growth rate, samples with more significant concentrations of cerium exhibited maximum cell survival and were protected against oxidative stress and death caused by hydrogen peroxide. The sol–gel synthesis technique enhanced the growth rate of the hydroxyapatite layer compared to the conventional melt-quenching

route. Zeta potential measurements indicate shifting surface charge signs with time when the samples were immersed in simulated bodily fluid, indicating the adsorption of cations and precipitation of phosphate ions.

Overall, the addition of Ce to the bioceramic samples improved their chemical durability and antioxidant capabilities, whereas the development rate of HA was impaired at higher Ce concentrations (Figure 4).

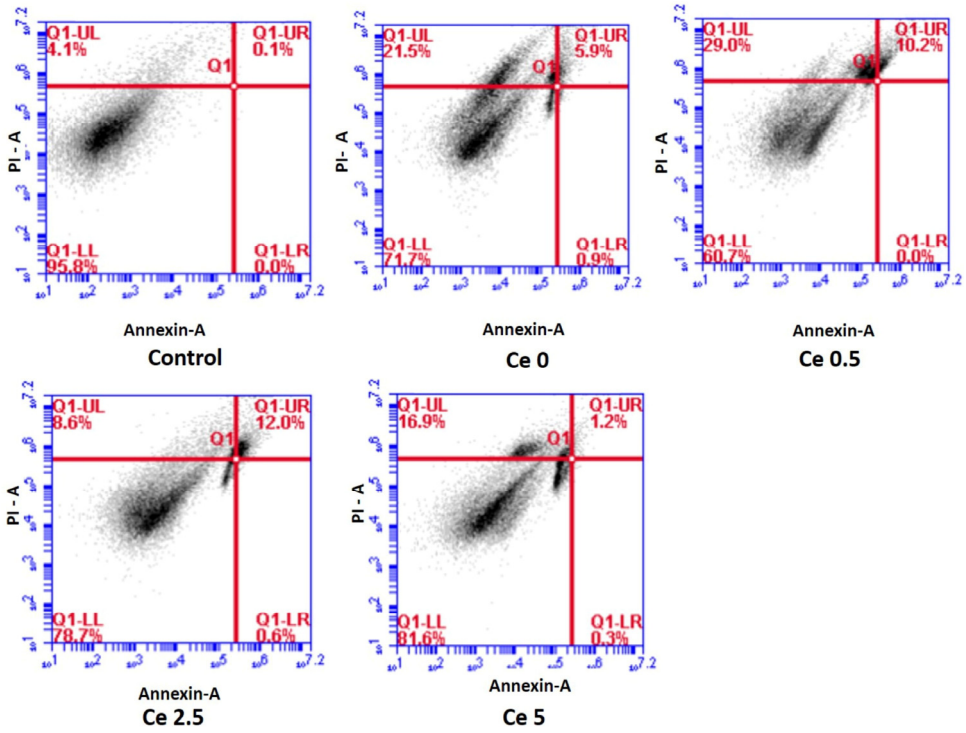

Figure 4. Apoptosis induction in MG-63 cells after 24 h treatment with test samples as analyzed using flow cytometry ((live cells (LL quadrant), early apoptotic (LR quadrant), late apoptotic (UR quadrant) and necrotic (UL quadrant)). Results indicate the maximum live cells for the Ce 5 sample (adapted with permission from Ref. [39]. Copyright 2019 Elsevier).

Conventional crystalline silicon solar cells (c-Si) have limitations in terms of energy loss, particularly the ineffective utilization of short-wavelength photons in the UV region [40]. To improve the efficiency of c-Si solar cells, the use of down-conversion (DC) [41,42], down-shifting (DS) [43–45], and up-conversion (UP) layers [40,46] in solar cells has received attention. DC layers can convert high-energy UV photons into lower-energy visible or near-infrared photons, thereby improving the performance of the solar cells. Rare-earth-doped phosphors, such as SiO_2 co-doped with Ce and Tb, have been explored as DC layers to enhance the performance of solar cells.

D. A. Kumi et al. (2020) examined the ideal mole percentage ratios of SiO_2–Ce^{3+} Tb^{3+}-based phosphors for achieving the highest emission intensity [47]. The nanophosphors were integrated into EVA films and placed as a DC layer over commercial silicon solar cells.

SiO_2 codoped with Ce and Tb was synthesized using an ultrasonification approach combined with the modified Strober method. The precursors were dissolved in ethanol, followed by the addition of tetraethyl orthosilicate and threefold distilled water to initiate precursor hydrolysis. The resulting precipitates were washed, dried, and annealed in a H_2/Ar atmosphere. The luminescent and optical properties of the produced phosphors were studied, and the phosphors were integrated into poly EVA films overlaid on a commercial silicon solar cell. The transmittance and UV absorption capability of the phosphor films were measured, and current density–voltage tests were performed on Si solar cells with and without the phosphor–EVA composite layers to evaluate the photocurrent efficiency.

SEM images revealed that the SiO_2-Ce^{3+} Tb^{3+} phosphor powder contained spherical particles with a size distribution ranging from approximately 25 to 275 nm and an average diameter of 148 nm. The phosphor films showed good transmittance (approximately 76%) and UV absorption capability compared with conventional poly EVA films. The photocurrent efficiency of the silicon solar cell improved when the phosphor–EVA composite layers were placed on top, with specific compositions exhibiting an increase in efficiency (2.39%) and others showing negligible decreases relative to that of plain EVA films (Figure 5).

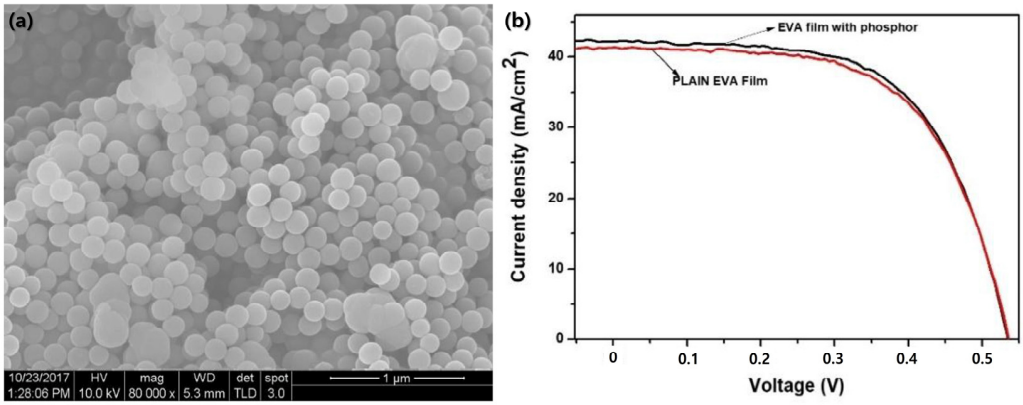

Figure 5. (**a**) SEM image of SiO_2 doped with Ce^{3+}, Tb^{3+}, and (**b**) current–voltage (I–V) curve for the sample which showed the highest increase in conversion efficiency with the poly EVA film layer (adapted with permission from Ref. [47]. Copyright 2019 Elsevier).

The study provides insights into the energy transmission between Ce and Tb ions in phosphors, which can be employed to adjust the composition of phosphor EVA composite films for enhanced performance in solar cell devices. The results of this study will contribute to the development of more efficient and cost-effective solar cell technologies that adopt DC layers to optimize the usage of short wavelength photons and improve the overall performance of c-Si solar cells.

As mentioned above, the Ce-doped cover glass studied by NASA is commercially available. Borosilicate glass doped with cerium dioxide is being used in space applications. It is used for UV, electron, and proton radiation protection, and its utilization is further enhanced by matching its thermal expansion coefficient to that of Si or GaAs [48]. G. Yang et al. (2016) analyzed the performance degradation of high-specific-power CdTe thin-film solar cells produced via high-energy proton irradiation [49]. The study identified uniformly distributed defects and optical transmittance loss as the main factors contributing to the reduction in cell performance, specifically in terms of current-level diminution, such as short-circuit current density (J_{SC}) (Figure 6). This is mainly owing to the transmittance loss caused by the darkening effect, as mentioned in the introduction.

To avoid performance degradation caused by the darkening effect, D. A. Lamb et al. (2017) introduced Ce-doped cover glasses as substrates for CdTe solar cells [50]. CdTe solar cells were directly fabricated on the Ce-doped cover glasses, and the CdTe devices were irradiated under various proton irradiation conditions. Consequently, at the lowest fluence of 10^{12} cm^{-2}, the relative efficiency of the solar cells was reduced by just 5%. This dosage of protons may plausibly be anticipated to represent that encountered by a 20-year geostationary Earth orbit (GEO) mission. Once the proton dosage was raised to 10^{13} cm^{-2} and 10^{14} cm^{-2}, the solar cell relative efficiency declined to 82% and 4%, respectively (Figure 7). This reaction to proton radiation was better than that observed in prior research employing CdTe and can be ascribed to the utilization of the Ce-doped cover glass. The degradation of CdTe solar cells owing to high-intensity proton doses was explained using SCAPS modeling. The 10^{13} cm^{-2} dose sample showed an excellent fit with a decrease in the acceptor concentration ($N_{a)}$ without any change in the trap density, which was unexpected but supported by the C-V measurements. This study provides insights into the effects of

proton irradiation on CdTe solar cells, including changes in carrier concentration, acceptor doping, and the formation of interstitial H^+ created by proton irradiation, resulting in shallow donor levels.

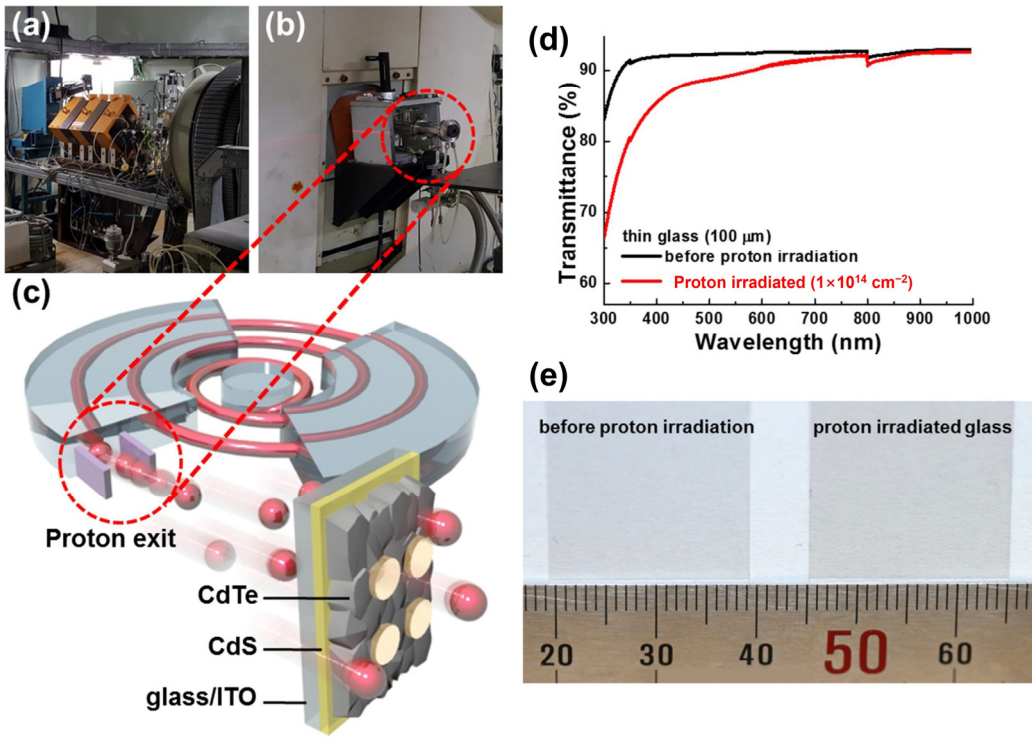

Figure 6. (**a**) Magnet for proton beam adjustment and (**b**) proton exit. (**c**) Schematic diagram of proton irradiation on CdS/CdTe solar cell grown on the ultra-thin glass substrate. (**d**) Transmittance graph and (**e**) photograph of 100 mm thick glass substrates before and after proton irradiation (15 MeV, 1×10^{14} cm^{-2}) (adapted with permission from Ref. [49]. Copyright 2016 Wiley-VCH).

Perovskite solar cells have drawn significant attention as potential alternatives to traditional silicon solar cells, owing to their high power conversion efficiency and low cost. Owing to their low cost and high specific power (Watt/gram) [51], they can replace conventional CdTe and Si photovoltaics in outer space applications. However, harsh conditions, such as the presence of high-energy particles, thermal cycling, and a vacuum, can lead to solar cell degradation in outer space. This degradation can cause ionization, atomic movement, and defects in the molecular structure, resulting in a decreased output and potential damage to semiconductor devices. Cyclic radiation, notably protons with energies close to 1 MeV, can cause severe damage to solar cells owing to their high-stop cross-section. To prevent damage to perovskite thin films, it is necessary to develop measures against proton collisions for space solar applications.

In 2015, proton radiation studies on PSCs were reported [52]. In 2016, F. Lang et al. reported that the irradiation of perovskite solar cells with protons with an energy of 68 MeV did not affect the open-circuit voltage (V_{oc}) and fill factor (FF). However, proton irradiation led to J_{sc} degradation, thus reducing the power conversion efficiency of the device (Figure 8a–c) [53]. In 2019, the same group evaluated the performance of superstrate-configuration (inverted structure) perovskite solar cells by irradiating protons with energies varying from 10 to 1000 MeV, instead of a single energy. They found that all PV parameters slightly decreased after proton irradiation (Figure 8d–f) [54]. Space solar cells use Ce-doped glass as a substrate; however, they are heavy and expensive. Ce-doped metal oxide is expected to protect space solar cells from GCR. As the specific power of space solar cells is essential to minimize their weight, a Ce-doped metal oxide deposited on a lightweight substrate can replace the current heavy space glasses. In addition, space solar

cells can be made flexible if Ce-doped metal oxides and perovskites are deposited onto flexible substrates.

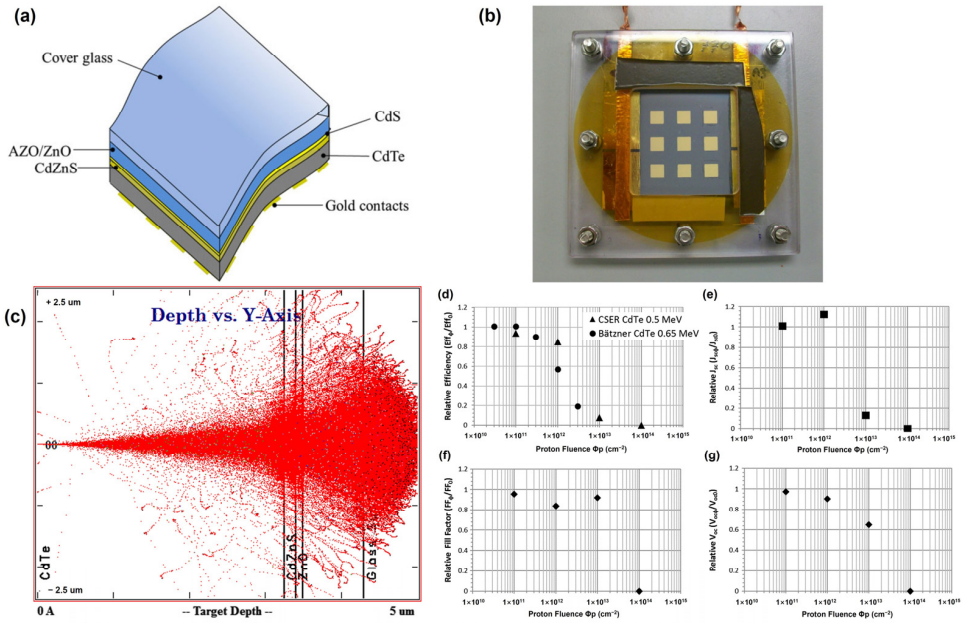

Figure 7. (**a**) Structure and (**b**) photograph in Perspex sample holder of CdTe solar cell on ultra-thin cerium-doped cover glass. (**c**) SRIM simulation of 0.5 MeV proton longitudinal penetration in the CdTe solar cell. Mean J-V parameters of each sample after proton irradiation, expressed as a ratio to unirradiated values versus proton fluence (cm^{-2}). (**d**) Mean efficiency; (**e**) mean J_{sc}; (**f**) mean V_{oc}; (**g**) mean FF.

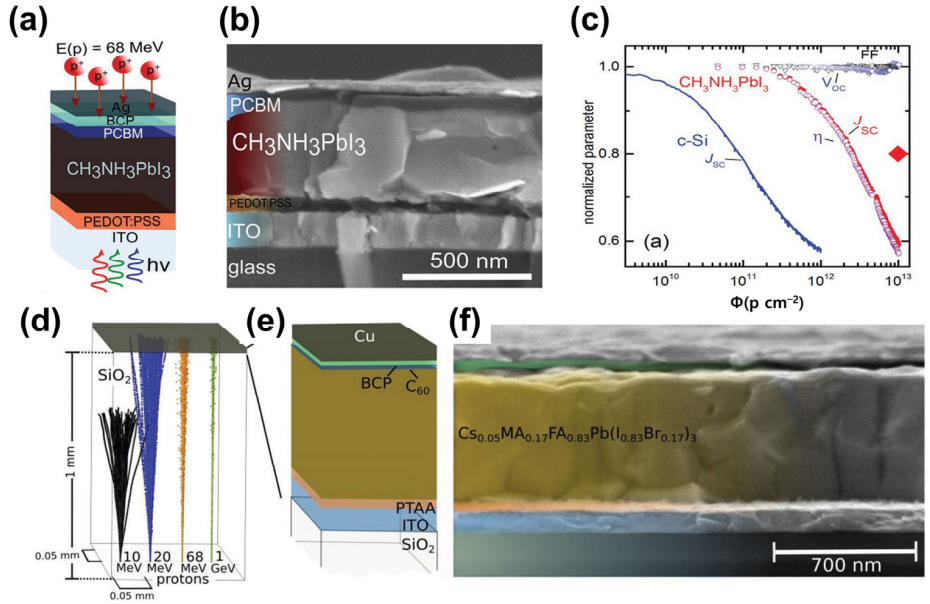

Figure 8. (**a**) Structural diagram of perovskite solar cell with glass/ITO/PEDOT:PSS/MALHs/PCBM/BCP/Ag structure, (**b**) SEM cross-sectional image, (**c**) PV parameter comparison with crystalline silicon device after proton irradiation (adapted with permission from Ref. [53]. Copyright 2016 Wiley-VCH), (**d**) simulation results of proton irradiation on SiO_2 thin film, (**e**) structure of glass/ITO/PTAA/CsMAFAPb/C60/BCP/Cu structure of a perovskite solar cell, and (**f**) SEM cross-sectional image (adapted with permission from Ref. [54]. Copyright 2019 RSC Publishing).

3. Ce-Doped ZnO

Zinc oxide (ZnO) is a white, odorless, tasteless, solid type II–VI semiconductor. It is relatively abundant and inexpensive to produce. ZnO has a wide bandgap (3.37 eV at room temperature [55]; therefore, it is transparent in the visible region of its spectrum. ZnO exhibits piezoelectric properties, indicating that it can generate a mechanically deformed electric field. Owing to its desirable characteristics, ZnO has been employed in various applications, such as optoelectronics [56–58], electronics [59–61], and healthcare [62,63]. Optoelectronic devices are widely used in LEDs, solar cells, and photodetectors. In addition, they are used in transistors and sensors. Ce can be doped into ZnO to provide better optoelectronic performance, and many studies have reported improved Ce-doped ZnO performance.

Khuili et al. (2022) discovered that doping ZnO with rare-earth elements has a substantial impact on its optoelectronic and magnetic properties, resulting in an enlarged bandgap and a shift in the Fermi level to the conduction band, indicating n-type features [64]. The electrical conductivity of doped ZnO increases, making it suitable for use in integrated optoelectronic devices. Furthermore, rare-earth dopants create significant magnetic moments in the doped ZnO, broadening their potential uses in spintronics. The band structure, partial density of states (PDOS), and total density of states (DOS) were calculated to comprehend the electronic properties of the doped ZnO compounds (Figure 9). The DFT and reflectivity spectra provided insights into the potential applications of Tm-, Yb-, and Ce-doped ZnO compounds in integrated optoelectronic devices, solar cells, and spintronics.

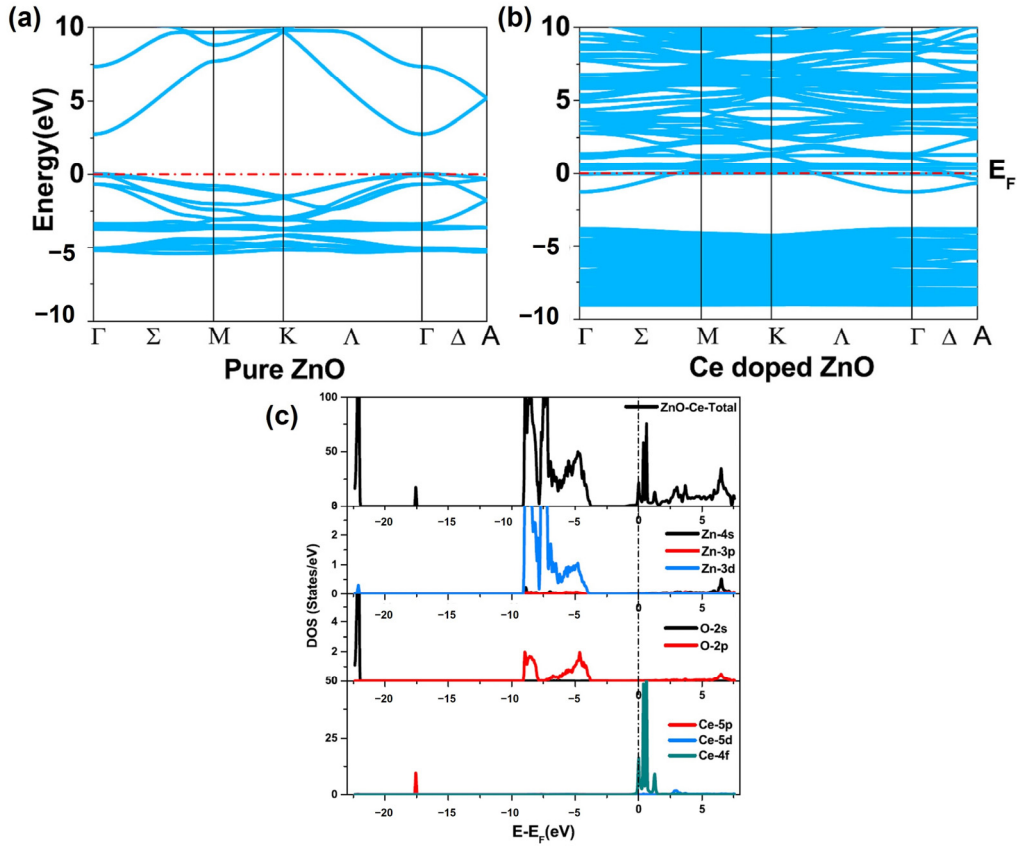

Figure 9. Band structure of (**a**) pure ZnO and (**b**) Ce-doped ZnO. (**c**) The partial density (PDOS) and total density of the states (TDOS) of pure and rare-earth-doped ZnO (adapted with permission from Ref. [64]. Copyright 2020 Elsevier).

Kulandaisamy et al. (2016) investigated the effect of Ce dopants on the acetone and ethanolamine sensing characteristics of ZnO, providing insights into the microstructural and sensing mechanisms of Ce-doped ZnO nanostructured films prepared using

spray pyrolysis [65]. Ce-doped ZnO thin films were deposited on a glass substrate via spray pyrolysis and characterized using XRD and SEM to determine their structural characteristics, lattice parameters, average crystallite size, and surface morphologies. They controlled the doping concentration with the precursor amount, and the Ce-doped ZnO thin films exhibited a decreased grain size and increased bandgap with an increase in the Ce dopant concentration. The sensors exhibited better RT sensing responses to acetone and ethanolamine at specific Ce dopant concentrations (Figure 10). The study demonstrates the potential of using Ce-doped ZnO sensors as a noninvasive and cost-effective method for disease detection with high selectivity to acetone and ethanolamine and swift response and recovery times.

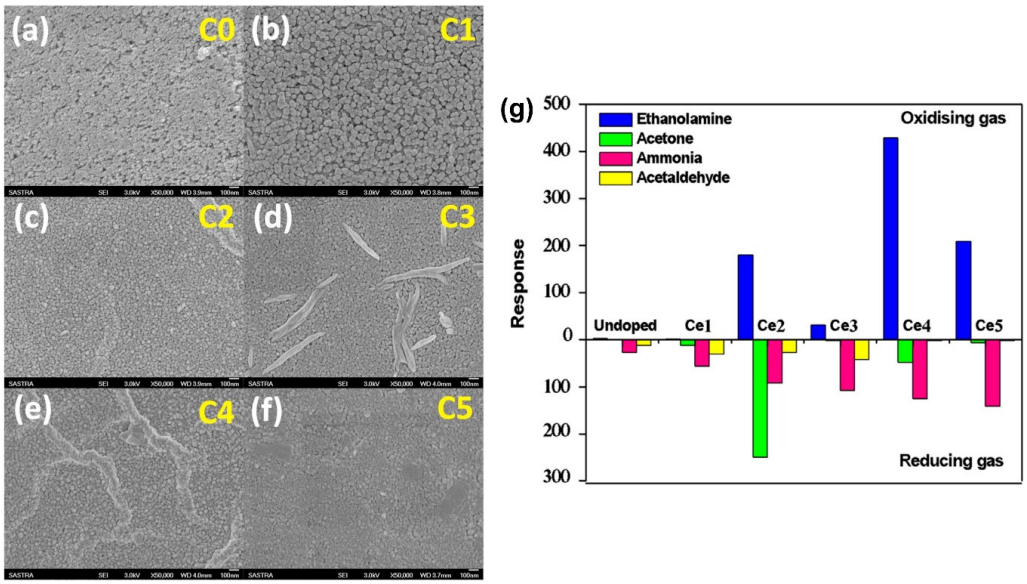

Figure 10. SEM images of undoped (**a**) and Ce-doped ZnO (**b**–**f**) samples, and (**g**) sensing response of undoped samples. Ce-doped ZnO samples to 100 ppm of ethanolamine, acetone, ammonia, and acetaldehyde vapors (adapted with permission from Ref. [65]. Copyright 2016 Elsevier).

Zhang et al. (2021) used a simple and controlled hydrothermal process to fabricate porous Ce-doped ZnO (CZO) nanosheets [66]. To prepare the CZO composites, different concentrations of Ce (0.5, 1, 3, and 5 at%) were doped into ZnO. This synthesis involves the substitution of Zn ions with Ce ions, which causes lattice deformation and the production of oxygen vacancy (OV) defects. The physical properties of the samples were evaluated using XRD, SEM, TEM, and AFM microscopy. The sensing capabilities, including their responsiveness and the selectivity of the CZO composites, were examined at RT. They found that the sensing capabilities of the sensors increased owing to the increased number of oxygen vacancies formed by Ce doping. Based on density functional theory (DFT) calculations, they discovered that Ce doping effectively reduced the band gap and increased the absorption energy between ZnO and aniline (Figure 11).

The OV in CZO has been shown to facilitate CO_2 adsorption and activation, suggesting that OV defect engineering can be used to improve CO_2 electrocatalytic reduction activity. Ce doping was utilized to introduce OV into ZnO, and the doping concentration of the Ce^{3+} dopant may have adjusted the concentration of OV in $Ce_xZn_{1-x}O$. Ren et al. (2021) proposed a method for generating high-performance CO_2 electrocatalytic reduction (ER) catalysts by varying the number of oxygen vacancies [67]. A hydrothermal technique was employed to fabricate the Ce-doped ZnO catalysts with different OV concentrations. The concentration of the Ce^{3+} dopant was varied to regulate the concentration of oxygen vacancies. The increased OV in Ce-doped ZnO improves CO_2 adsorption, lowers the thermodynamic energy barrier, and accelerates electron transfer kinetics during CO_2 ER (Figure 12). The use of Ce-doped ZnO catalysts with regulated OV concentrations can help

produce efficient and selective CO_2 reduction electrocatalysts, most likely enabling CO_2 conversion into valuable fuels to reduce climate change.

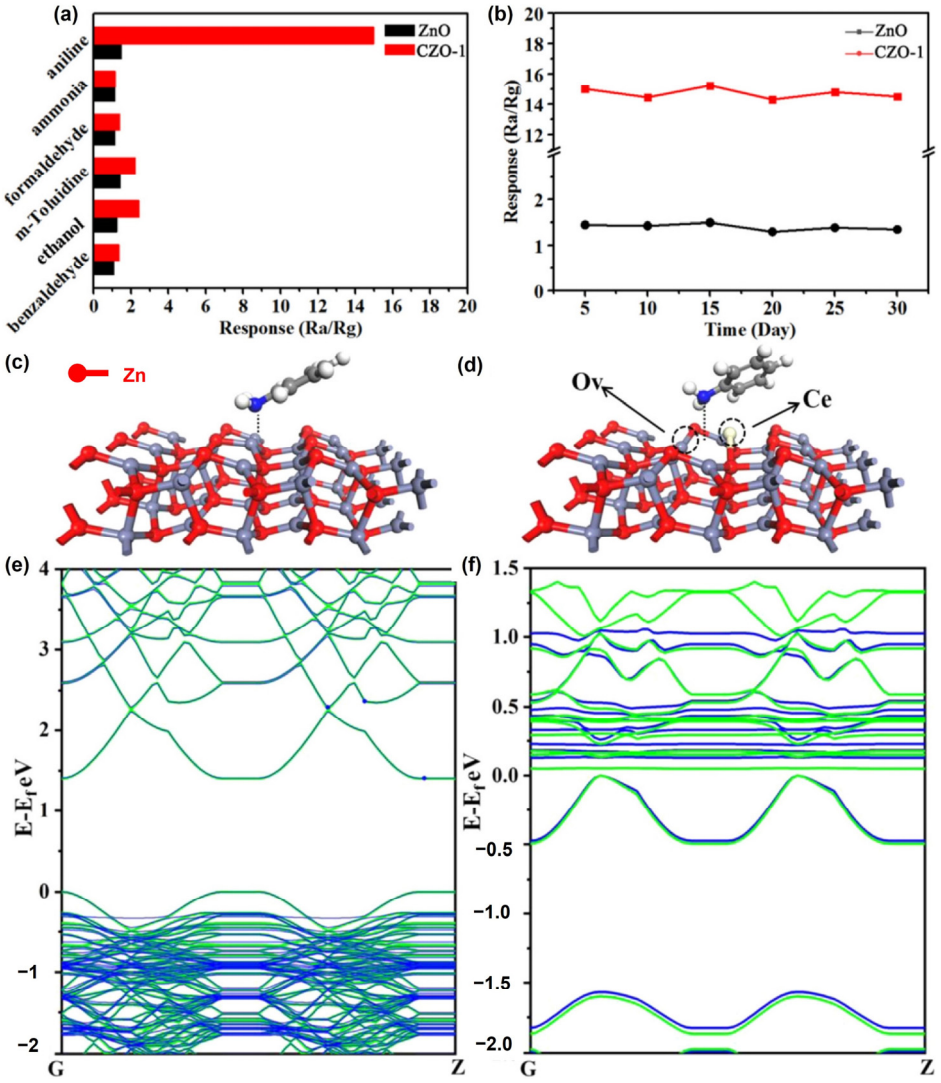

Figure 11. (**a**) Response of pristine ZnO and CZO-1 to various gases at RT. (**b**) Long-term pure ZnO and CZO-1 aniline stability at room temperature. The favorable configurations of (**c**) ZnO@aniline and (**d**) OV-CZO@aniline. (**e**) Band structures for pristine ZnO (green) and ZnO@aniline (blue). (**f**) Band structures for OV-CZO (green) and OV-CZO@aniline (blue) (adapted with permission from Ref. [66]. Copyright 2021 Elsevier).

UV photodetectors (PDs) are essential for various applications, including sensors, military defense, and optical communications [68–70]. ZnO is a promising material for UV PDs owing to its outstanding features, such as large carrier concentration, significant absorption coefficient, and acceptable bandgap [71]. Doping ZnO with Ce can boost its performance by decreasing the carrier recombination [72]. However, the effect of Ce on the UV photoresponse of ZnO is yet to be established.

M. Shkir et al. (2022) explored Ce-doped ZnO thin-film devices for UV photodetection [73]. Spray pyrolysis can be used to produce ZnO photodetectors with varying wt.% values of Ce dopants. The Zn and Ce precursors were dissolved in water, mixed, and coated onto pre-cleaned glass via spray pyrolysis. During film deposition, the temperature of the glass substrate was uniformly controlled at 450 °C via a temperature controller. The 2D piston motion in both the x- and y-dimensions and the spraying conditions were accurately controlled by software.

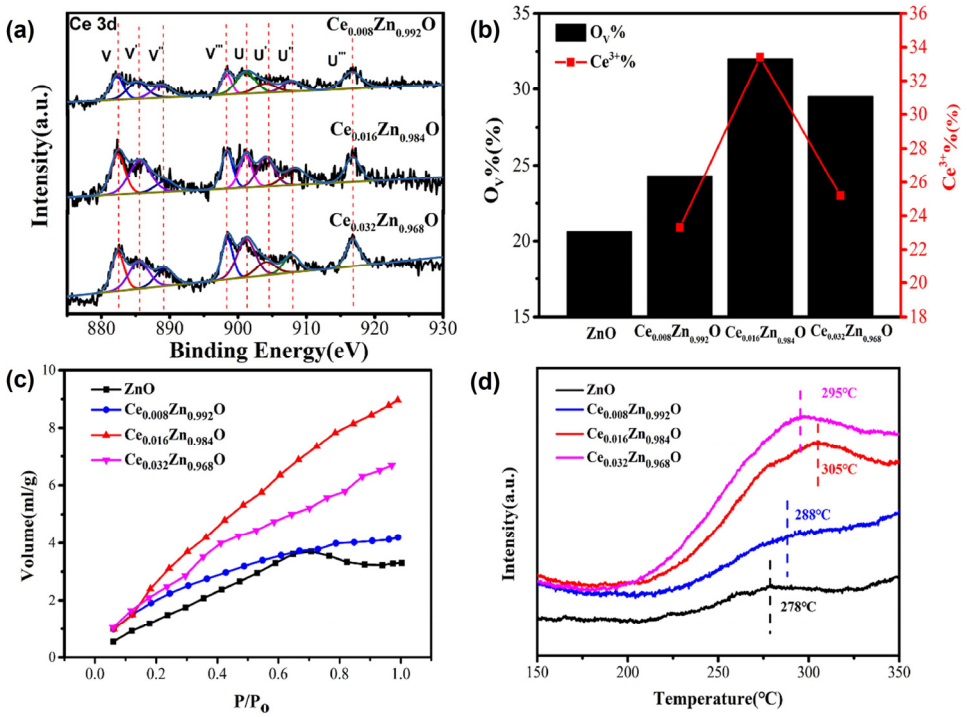

Figure 12. (**a**) Ce 3d XPS spectra of $Ce_xZn_{1-x}O$, (**b**) the calculated ratio of integral areas for the OV, (**c**) CO_2 adsorption isotherms at 25 °C and (**d**) CO_2-TPD spectra (adapted with permission from Ref. [67]. Copyright 2021 Elsevier).

An evaluation of the UV detection capabilities of the constructed devices showed that the ZnO:Ce(2.0%) sample displayed good UV photodetection properties, with a maximum responsivity of 0.27 A/W, detectivity of 63%, and external quantum efficiency of 2.18×10^{10} Jones. This highlights their potential use as UV photodetectors. The photoresponse results showed that the current increased with increasing Ce concentrations and was saturated at 2 wt%, indicating the higher conductivity of ZnO:Ce(2.0). The optical characteristics of ZnO were altered by Ce doping, as the dopant altered the electronic structure. The absorption spectra indicate the influence of Ce on the optical properties of ZnO. The topographies and morphologies of the ZnO and ZnO:Ce films were examined using AFM. Ce doping altered the surface topography, with the ZnO:Ce(2.0) film showing uniformly sized grains without any fissures.

The fast transfer of photogenerated charge carriers was enabled by the ohmic contact between the ZnO device and the Ag electrode, contributing to the short response and recovery times of the devices. The photodetection mechanism involved interactions between the excitons and O_2 ions in the depletion layer, contributing to the improved performance of the ZnO:Ce devices (Figure 13). These promising device properties, including responsivity, detectivity, and EQE, render the ZnO:Ce(2.0%) sample a potential candidate for UV photodetection applications.

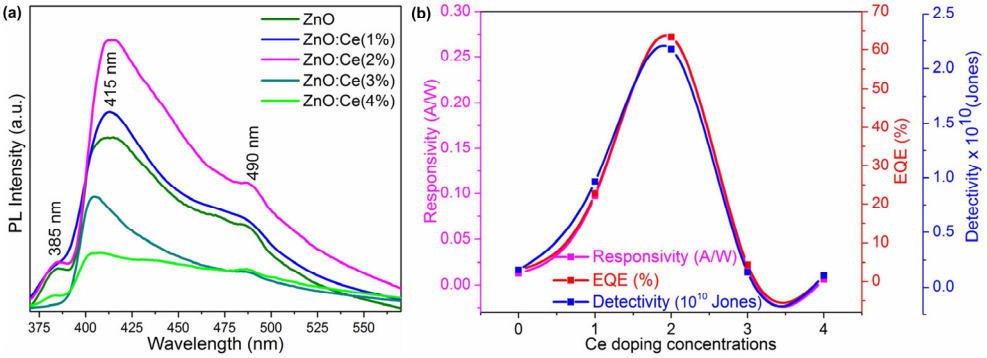

Figure 13. (**a**) Photoluminescence spectra of ZnO and ZnO:Ce thin films and (**b**) responsivity, EQE, and the detectivity of the fabricated ZnO and Ce:ZnO devices (adapted with permission from Ref. [73]. Copyright 2022 Elsevier).

Ce-doped ZnO nanowires have the potential to be used in water treatment. Semiconductor metal oxides, such as TiO_2 and ZnO, have been extensively used for photocatalytic treatment because of their excellent photodegradation activity, high abundance, low cost, non-toxicity, and high stability [74–76]. However, ZnO semiconductors have limitations owing to their broad bandgap energy, which limits their photocatalytic capabilities [77,78]. Doping ZnO nanostructures with rare-earth metals has been shown to be useful because it boosts the light absorption capabilities and the separation of charge carriers.

S. Choudhary et al. (2023) investigated a simple and rapid process for fabricating Ce-doped ZnO nanowires using a thermal decomposition approach [79]. Moreover, they discussed the impact of the Ce doping concentration on the lattice characteristics, crystallite size, and light absorption capacity. Ce-doped ZnO nanowire manufacturing involves thermal decomposition using zinc acetate and cerium nitrate as precursor ingredients. A mixture of the precursor salt and cerium dopant is blended to achieve a final weight of 2 g. The mixture is then transferred to alumina crucibles for thermal treatment at 350 °C for 30 min in a muffle furnace. The off-white powder elements are finely pulverized using a mortar and pestle. Pure ZnO samples are classified as ZPW, while samples containing a variable Ce dopant are denoted as ZCW1 (Ce 0.5 wt%), ZCW2 (Ce 1 wt%), and ZCW3(Ce 1.5 wt%). The impact of cerium doping on the nanowire structure, optical characteristics, and photodegradation behavior was studied using XRD, FE-SEM, Raman spectroscopy, XPS, PL, and UV-vis absorption spectroscopy. The photocatalytic response of the nanowires was tested for the degradation of cationic and anionic dyes, and the photodecomposition efficiency was calculated.

Ce-doped ZnO nanowires displayed remarkable photodegradation efficacy in the removal of organic contaminants from water. ZnO nanowires doped with 0.5% Ce demonstrated the best photodecolorization performance, with photodecomposition efficiencies of 96.6% for MB, 92.2% for MG, 67.1% for MO, and 77.7% for RhB dye removal in 16 min of sunlight exposure (Figure 14a). The strain of the produced samples was estimated using the Williamson–Hall equation, which provides information on the lattice spacing and crystallite size.

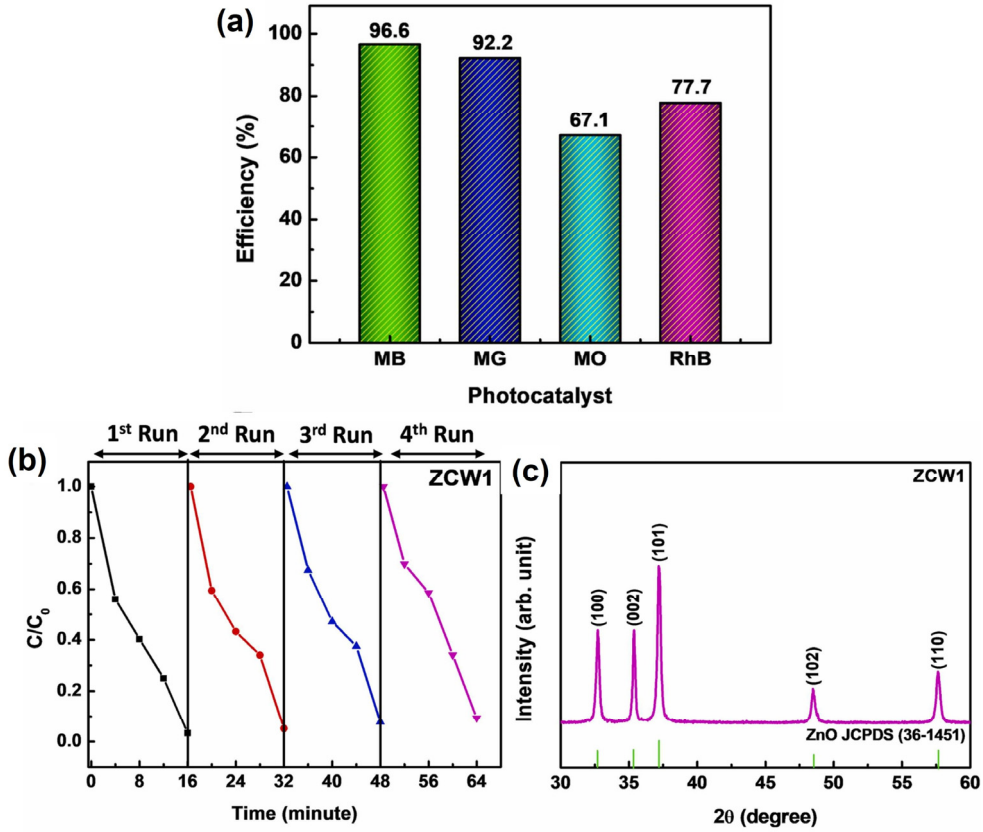

Figure 14. (**a**) Decomposition efficiencies of the ZCW1 sample in the removal of various organic dyes, (**b**) recyclability of ZnO nanowires doped with Ce in sample ZCW1 for four successive cycles to the photodecomposition of MB under sunlight irradiation, and (**c**) XRD patterns of the ZCW1 photocatalyst after undergoing repetitive photocatalytic treatments under identical experimental conditions (adapted with permission from Ref. [79]. Copyright 2022 Elsevier).

The remarkable reusability and stability of the nanowires further enhance their practical use in wastewater treatment systems (Figure 14b,c). Utilizing the thermal decomposition approach for the synthesis of Ce-doped ZnO nanowires provides a facile and rapid method for their manufacture, which can be extended to large-scale manufacturing.

4. Conclusions

Ce-doped materials, specifically Ce-doped SiO_2 and ZnO, have shown promising results in various optoelectronic applications. Ce-doped SiO_2 has been studied for its UV and X-ray shielding properties, light emission, and proton protection in space applications. Ce-doped SiO_2 thin films have been found to exhibit luminescence in the visible-near-infrared range, and their luminescence behavior can be controlled by altering the Ce content and annealing temperature. Incorporating Ce^{3+} ions into a borosilicate glass matrix improved the green emission of the nanocrystal–glass composite and increased the X-ray-stimulated luminescence intensity. Ce doping has also been used to improve the chemical stability and antioxidant capabilities of bioceramics, the short-circuit current of c-Si solar cells, and the OSL and TSL of RPL materials. A Ce-doped cover glass can be utilized as a substrate for CdTe solar cells to alleviate the performance degradation caused by high-energy proton irradiation. The relative efficiency of the solar cells was reduced by only 5% at the lowest fluence of protons, and even at higher doses, the degradation was better than that in previous research on CdTe without Ce-doped glass.

Ce-doped ZnO has been investigated owing to its improved optoelectronic and magnetic properties. Doping ZnO with rare-earth elements, including Ce, has been found to increase the bandgap and electrical conductivity of ZnO, making it suitable for inte-

grated optoelectronic devices and spintronics. Ce-doped ZnO has also shown potential for gas sensing applications with improved sensing characteristics for sensing acetone and ethanolamine. The sensing capabilities of Ce-doped ZnO sensors can be further enhanced by increasing the Ce concentration, which creates increased oxygen vacancies and improves the responsiveness and selectivity. Doping ZnO with 2 wt% Ce resulted in a 63% improvement in UV detection performance over the undoped sample, and doping the nanowire-shaped sample demonstrated its performance as a reusable water treatment material. Table 1 summarizes the research on various applications of Ce-doped SiO_2 and ZnO introduced in this paper.

Table 1. Summary of Ce-doped SiO_2 and ZnO research results for various applications.

Materials	Applications	Purpose	Results	Fabrication Method	Ref.
Ce doped SiO_2	Optoelectronic	Tuning of optical properties	strong blue luminescence at room temperature	Co-evaporation	[31]
		luminescence characteristics	vigorous luminous intensity and reasonably high transmittance (80% at 527 nm)	Melt quenching	[32]
			a strong band emission in the UV-blue range due to Mie scattering	spark plasma sintering	[35]
	Biomedical	chemical durability and antioxidant capabilities	a decrease in growth rate of HA and protection against the H_2O_2 stress	Sol-gel	[39]
	Photovoltaic	Improvement of solar cell efficiency	2.39% efficiency increase in the c-Si solar cell applied to the EVA	Strober method	[47]
		proton radiation protection	5% relative efficiency decrease in the solar cells at a proton fluence of 10^{12}cm^{-2}	Commercial product	[50]
Ce doped ZnO	Principle	Analysis of optoelectronic and magnetic properties	Identification of changes in the optoelectronic and magnetic properties of ZnO due to the presence of 4f electrons originating from rare earth element doping	Simulation	[64]
	Gas sensor	acetone and ethanolamine sensing	acetone response (S = 252 for 500 ppm) ethanolamine response (S = 1850 for 500 ppm)	spray pyrolysis	[65]
		aniline sensing	aniline response (S = 15.1 for 100 ppm)	hydrothermal	[66]
		electrocatalytic CO_2 reduction to CO	current density of 24 mA cm^{-2} and Faradaic efficiency of 88% for CO at −1.0 V versus RHE	hydrothermal	[67]
	Optoelectronic	UV detection	UV responsivity: 0.27 A/W; detectivity: 63%; EQE: 2.18 × 10^{10} Jones.	Spray pyrolysis	[73]
	Water treatment	removal of various organic dyes	Improvement in decomposition efficiencies in removal of various organic dyes	thermal decomposition	[79]

Overall, Ce-doped materials, such as Ce-doped SiO_2 and Ce-doped ZnO, have great potential in various fields, including radiation shielding, light emission, and gas sensing. Further research and development in these areas could lead to advanced materials with customized optical and electrical properties for various applications. Overall, the commercialization of Ce-doped SiO_2 and ZnO is still in its early stages. However, growing interest in the industry and investment in technology development suggest that these materials have the potential to be widely used in the future.

Author Contributions: Investigation and resources, M.C.; writing—original draft preparation and visualization, S.K., writing—review and editing, supervision, J.P. All authors have read and agreed to the published version of the manuscript.

Funding: This research was funded by the National Research Foundation of Korea, grant number RS-2023-00257494.

Data Availability Statement: Not applicable.

Acknowledgments: This research was supported by the Basic Science Research Program through the National Research Foundation of Korea (NRF) funded by the Ministry of Education (NRF-2022R1I1A3069502), and this work was supported by the National Research Foundation of Korea (NRF) grant funded by the Korean government (MEST) (RS-2023-00257494).

Conflicts of Interest: The authors declare no conflict of interest.

References

1. Zhang, J.; Peng, W.; Chen, Z.; Chen, H.; Han, L. Effect of cerium doping in the TiO_2 photoanode on the electron transport of dye-sensitized solar cells. *J. Phys. Chem. C* **2012**, *116*, 19182–19190. [CrossRef]
2. Srisuvetha, V.; Rayar, S.; Shanthi, G. Role of cerium (Ce) dopant on structural, optical and photocatalytic properties of MgO nanoparticles by wet chemical route. *J. Mater. Sci.-Mater. Electron.* **2020**, *31*, 2799–2808. [CrossRef]
3. Xu, J.; Ao, Y.; Fu, D. A novel Ce, C-codoped TiO_2 nanoparticles and its photocatalytic activity under visible light. *Appl. Surf. Sci.* **2009**, *256*, 884–888. [CrossRef]
4. Zhang, Y.; Yuwono, A.H.; Wang, J.; Li, J. Enhanced photocatalysis by doping cerium into mesoporous titania thin films. *J. Phys. Chem. C* **2009**, *113*, 21406–21412. [CrossRef]
5. Chen, S.; Lee, J.; Lu, K.; Pao, C.; Lee, J.; Chan, T.; Chen, J. Band-gap narrowing of TiO_2 doped with Ce probed with X-ray absorption spectroscopy. *Appl. Phys. Lett.* **2010**, *97*, 012104. [CrossRef]
6. Fu, C.; Li, T.; Qi, J.; Pan, J.; Chen, S.; Cheng, C. Theoretical study on the electronic and optical properties of Ce^{3+}-doped TiO_2 photocatalysts. *Chem. Phys. Lett.* **2010**, *494*, 117–122. [CrossRef]
7. Keating, P.R.; Scanlon, D.O.; Morgan, B.J.; Galea, N.M.; Watson, G.W. Analysis of intrinsic defects in CeO_2 using a Koopmans-like GGA+ U approach. *J. Phys. Chem. C* **2012**, *116*, 2443–2452. [CrossRef]
8. Nyoka, M.; Choonara, Y.E.; Kumar, P.; Kondiah, P.P.; Pillay, V. Synthesis of cerium oxide nanoparticles using various methods: Implications for biomedical applications. *Nanomaterials* **2020**, *10*, 242. [CrossRef]
9. Lin, Y.-H.; Shen, L.-J.; Chou, T.-H.; Shih, Y.-H. Synthesis, stability, and cytotoxicity of novel cerium oxide nanoparticles for biomedical applications. *J. Clust. Sci.* **2021**, *32*, 405–413. [CrossRef]
10. Gallucci, N.; Vitiello, G.; Di Girolamo, R.; Imbimbo, P.; Monti, D.M.; Tarallo, O.; Vergara, A.; Russo Krauss, I.; Paduano, L. Towards the development of antioxidant cerium oxide nanoparticles for biomedical applications: Controlling the properties by tuning synthesis conditions. *Nanomaterials* **2021**, *11*, 542. [CrossRef]
11. Singh, K.R.; Nayak, V.; Sarkar, T.; Singh, R.P. Cerium oxide nanoparticles: Properties, biosynthesis and biomedical application. *RSC Adv.* **2020**, *10*, 27194–27214. [CrossRef]
12. Pang, A.; Li, J.; Wei, X.-F.; Ruan, Z.-W.; Yang, M.; Chen, Z.-N. UV–O_3 treated annealing-free cerium oxide as electron transport layers in flexible planar perovskite solar cells. *Nanoscale Adv.* **2020**, *2*, 4062–4069. [CrossRef]
13. Al-Mousoi, A.K.; Mohammed, M.K.; Pandey, R.; Madan, J.; Dastan, D.; Ravi, G.; Sakthivel, P. Simulation and analysis of lead-free perovskite solar cells incorporating cerium oxide as electron transporting layer. *RSC Adv.* **2022**, *12*, 32365–32373. [CrossRef]
14. Mehmood, U.; Ahmad, S.; Al-Ahmed, A.; Hakeem, A.S.; Dafalla, H.; Laref, A. Synthesis and characterization of cerium oxide impregnated titanium oxide photoanodes for efficient dye-sensitized solar cells. *IEEE J. Photovolt.* **2020**, *10*, 1365–1370. [CrossRef]
15. Seal, S.; Jeyaranjan, A.; Neal, C.J.; Kumar, U.; Sakthivel, T.S.; Sayle, D.C. Engineered defects in cerium oxides: Tuning chemical reactivity for biomedical, environmental, & energy applications. *Nanoscale* **2020**, *12*, 6879–6899. [PubMed]
16. Koettgen, J.; Martin, M. The ionic conductivity of Sm-doped ceria. *J. Am. Ceram. Soc.* **2020**, *103*, 3776–3787. [CrossRef]
17. Zeng, D.; Kang, F.; Qiu, Y.; Cui, D.; Li, M.; Ma, L.; Zhang, S.; Xiao, R. Iron oxides with gadolinium-doped cerium oxides as active supports for chemical looping hydrogen production. *Chem. Eng. J.* **2020**, *396*, 125153. [CrossRef]
18. Accardo, G.; Audasso, E.; Yoon, S.P. Unravelling the synergistic effect on ionic transport and sintering temperature of nanocrystalline CeO_2 tri-doped with Li Bi and Gd as dense electrolyte for solid oxide fuel cells. *J. Alloys Compd.* **2022**, *898*, 162880. [CrossRef]
19. Lu, Y.; Zhu, B.; Shi, J.; Yun, S. Advanced low-temperature solid oxide fuel cells based on a built-in electric field. *Energy Mater* **2022**, *1*, 100007. [CrossRef]
20. Jing, Y.; Lund, P.; Asghar, M.I.; Li, F.; Zhu, B.; Wang, B.; Zhou, X.; Chen, C.; Fan, L. Non-doped CeO_2-carbonate nanocomposite electrolyte for low temperature solid oxide fuel cells. *Ceram. Int.* **2020**, *46*, 29290–29296. [CrossRef]
21. Jain, B.; Singh, A.K.; Hashmi, A.; Susan, M.A.B.H.; Lellouche, J.-P. Surfactant-assisted cerium oxide and its catalytic activity towards Fenton process for non-degradable dye. *Adv. Compos. Hybrid Mater.* **2020**, *3*, 430–441. [CrossRef]
22. Sugiura, M. Oxygen storage materials for automotive catalysts: Ceria-zirconia solid solutions. *Catal. Surv. Asia* **2003**, *7*, 77–87. [CrossRef]
23. Grabchenko, M.V.; Mamontov, G.V.; Zaikovskii, V.I.; La Parola, V.; Liotta, L.F.; Vodyankina, O.V. The role of metal–support interaction in Ag/CeO_2 catalysts for CO and soot oxidation. *Appl. Catal. B Environ.* **2020**, *260*, 118148. [CrossRef]
24. Mishra, U.K.; Chandel, V.S.; Singh, O.P. A review on cerium oxide–based catalysts for the removal of contaminants. *Emergent Mater.* **2022**, *5*, 1443–1476. [CrossRef]

25. Hebert, S.C.; Stöwe, K. Synthesis and characterization of bismuth-cerium oxides for the catalytic oxidation of diesel soot. *Materials* **2020**, *13*, 1369. [CrossRef]
26. White, R.H.; Wirtenson, G.R. *Radiation Induced Darkening of the Optical Elements in the Startracker Camera*; Lawrence Livermore National Lab (LLNL): Livermore, CA, USA, 1993.
27. Teng, L.; Jiang, Y.; Zhang, W.; Wei, R.; Guo, H. Highly transparent cerium doped glasses with full-band UV-shielding capacity. *J. Am. Ceram. Soc.* **2020**, *103*, 3249–3256. [CrossRef]
28. Cong, W.-Y.; Lu, Y.-B.; Zhang, P.; Guan, C.-B. First principle study of electronic structures and optical properties of Ce-doped SiO_2. *AIP Adv.* **2018**, *8*, 055125. [CrossRef]
29. Stroud, J.S. Photoionization of Ce^{3+} in glass. *J. Chem. Phys.* **1961**, *35*, 844–850. [CrossRef]
30. Haynes, G.A. *Effect of Radiation on Cerium-Doped Solar-Cell Cover Glass*; National Aeronautics and Space Administration: Washington, DC, USA, 1970.
31. Weimmerskirch-Aubatin, J.; Stoffel, M.; Bouché, A.; Boulet, P.; Vergnat, M.; Rinnert, H. Optical properties of Ce-doped SiO_2 films: From isolated Ce^{3+} ions to formation of cerium silicate. *J. Alloys Compd.* **2015**, *622*, 358–361. [CrossRef]
32. Su, M.L.; Zhang, Q.; Gao, Y.J.; Chen, C.; Wei, W. Enhanced luminescence of $CsPbBr_3$ nanocrystals-glass composite scintillators based on Ce^{3+}-doped borosilicate glass. *J. Lumin.* **2022**, *242*, 118553. [CrossRef]
33. Wang, C.; Lin, H.; Zhang, Z.; Qiu, Z.; Yang, H.; Cheng, Y.; Xu, J.; Xiang, X.; Zhang, L.; Wang, Y. X-ray excited CsPb $(Cl, Br)_3$ perovskite quantum dots-glass composite with long-lifetime. *J. Eur. Ceram. Soc.* **2020**, *40*, 2234–2238. [CrossRef]
34. Sun, X.-Y.; Xiao, Z.-H.; Wu, Y.-T.; Kang, Z. Fast Ce3+-activated borosilicate glass scintillators prepared in air atmosphere. *Ceram. Int.* **2017**, *43*, 3401–3404. [CrossRef]
35. Okada, G.; Kasap, S.; Yanagida, T. Optically-and thermally-stimulated luminescences of Ce-doped SiO_2 glasses prepared by spark plasma sintering. *Opt. Mater.* **2016**, *61*, 15–20. [CrossRef]
36. Sobek, J.M.; Talburt, D.E. Effects of the rare earth cerium on Escherichia coli. *J. Bacteriol.* **1968**, *95*, 47–51. [CrossRef]
37. Rygel, J.L.; Pantano, C. Synthesis and properties of cerium aluminosilicophosphate glasses. *J. Non-Cryst. Solids* **2009**, *355*, 2622–2629. [CrossRef]
38. Zhang, X.; Kehoe, S.; Adhi, S.; Ajithkumar, T.; Moane, S.; O'shea, H.; Boyd, D. Composition–structure–property (Zn^{2+} and Ca^{2+} ion release) evaluation of Si–Na–Ca–Zn–Ce glasses: Potential components for nerve guidance conduits. *Mater. Sci. Eng. C* **2011**, *31*, 669–676. [CrossRef]
39. Kaur, P.; Singh, K.; Yadav, A.K.; Kaur, S.; Kaur, R.; Kaur, S. Growth of bone like hydroxyapatite and cell viability studies on CeO_2 doped CaO–P_2O_5–MgO–SiO_2 bioceramics. *Mater. Chem. Phys.* **2020**, *243*, 122352. [CrossRef]
40. Shang, Y.; Hao, S.; Yang, C.; Chen, G. Enhancing solar cell efficiency using photon upconversion materials. *Nanomaterials* **2015**, *5*, 1782–1809. [CrossRef]
41. Abrams, Z.E.R.; Niv, A.; Zhang, X. Solar energy enhancement using down-converting particles: A rigorous approach. *J. Appl. Phys.* **2011**, *109*, 114905. [CrossRef]
42. Badescu, V.; De Vos, A.; Badescu, A.M.; Szymanska, A. Improved model for solar cells with down-conversion and down-shifting of high-energy photons. *J. Phys. D Appl. Phys.* **2007**, *40*, 341. [CrossRef]
43. Van Sark, W. Simulating performance of solar cells with spectral downshifting layers. *Thin Solid Film.* **2008**, *516*, 6808–6812. [CrossRef]
44. Ho, W.-J.; Shen, Y.-T.; Deng, Y.-J.; Yeh, C.-W.; Sue, R.-S. Performance enhancement of planar silicon solar cells through utilization of two luminescent down-shifting Eu-doped phosphor species. *Thin Solid Film.* **2016**, *618*, 141–145. [CrossRef]
45. Klampaftis, E.; Ross, D.; McIntosh, K.R.; Richards, B.S. Enhancing the performance of solar cells via luminescent down-shifting of the incident spectrum: A review. *Sol. Energy Mater. Sol. Cells* **2009**, *93*, 1182–1194. [CrossRef]
46. Goesmann, H.; Feldmann, C. Nanoparticulate functional materials. *Angew. Chem. Int. Ed.* **2010**, *49*, 1362–1395. [CrossRef] [PubMed]
47. Kumi, D.O.; Khan, S.; Cho, S.-H.; Ntwaeaborwa, M.O. Ultraviolet to visible down conversion of SiO_2–Ce^{3+}, Tb^{3+} nanospheres-poly-EVA films for solar cell application. *Phys. B Condens. Matter* **2020**, *576*, 411711. [CrossRef]
48. Enabling the Future through Light. Available online: https://www.excelitas.com/product/space-qualified-cover-glass (accessed on 1 October 2023).
49. Yang, G.; Cho, E.W.; Hwang, Y.J.; Min, B.K.; Kang, Y.; Kim, D.; Kim, J. Radiation-Hard and Ultralightweight Polycrystalline Cadmium Telluride Thin-Film Solar Cells for Space Applications. *Energy Technol.* **2016**, *4*, 1463–1468. [CrossRef]
50. Lamb, D.A.; Underwood, C.I.; Barrioz, V.; Gwilliam, R.; Hall, J.; Baker, M.A.; Irvine, S.J. Proton irradiation of CdTe thin film photovoltaics deposited on cerium-doped space glass. *Prog. Photovolt.* **2017**, *25*, 1059–1067. [CrossRef]
51. Yang, S.; Xu, Z.; Xue, S.; Kandlakunta, P.; Cao, L.; Huang, J. Organohalide lead perovskites: More stable than glass under gamma-ray radiation. *Adv. Mater.* **2019**, *31*, 1805547. [CrossRef] [PubMed]
52. Miyazawa, Y.; Ikegami, M.; Miyasaka, T.; Ohshima, T.; Imaizumi, M.; Hirose, K. Evaluation of radiation tolerance of perovskite solar cell for use in space. In Proceedings of the 2015 IEEE 42nd Photovoltaic Specialist Conference (PVSC), New Orleans, LA, USA, 14–19 June 2015; pp. 1–4.
53. Lang, F.; Nickel, N.H.; Bundesmann, J.; Seidel, S.; Denker, A.; Albrecht, S.; Brus, V.V.; Rappich, J.; Rech, B.; Landi, G. Radiation hardness and self-healing of perovskite solar cells. *Adv. Mater.* **2016**, *28*, 8726–8731. [CrossRef]

54. Lang, F.; Jošt, M.; Bundesmann, J.; Denker, A.; Albrecht, S.; Landi, G.; Neitzert, H.-C.; Rappich, J.; Nickel, N.H. Efficient minority carrier detrapping mediating the radiation hardness of triple-cation perovskite solar cells under proton irradiation. *Energy Environ. Sci.* **2019**, *12*, 1634–1647. [CrossRef]
55. Tan, S.T.; Chen, B.; Sun, X.; Fan, W.; Kwok, H.S.; Zhang, X.; Chua, S. Blueshift of optical band gap in ZnO thin films grown by metal-organic chemical-vapor deposition. *J. Appl. Phys.* **2005**, *98*, 013505. [CrossRef]
56. El Jouad, M.; Touhtouh, S.; Addou, M.; Ollier, N.; Sahraoui, B. Red luminescence and UV light generation of europium doped zinc oxide thin films for optoelectronic applications. *Eur. Phys. J. Appl. Phys.* **2020**, *91*, 10501. [CrossRef]
57. Shkir, M.; Chandekar, K.V.; Alshehri, B.M.; Khan, A.; AlFaify, S.; Hamdy, M.S. A remarkable enhancement in photocatalytic activity of facilely synthesized Terbium@ Zinc oxide nanoparticles by flash combustion route for optoelectronic applications. *Appl. Nanosci.* **2020**, *10*, 1811–1823. [CrossRef]
58. Furhan; Ramesan, M.T. High performance optical and electrical properties of zinc oxide reinforced poly (diphenylamine) nanocomposites for optoelectronic applications. *Polym. Eng. Sci.* **2022**, *62*, 3418–3432. [CrossRef]
59. Suganthi, K.; Harish, K.; Nair, N.M.; Swaminathan, P. Formulation and optimization of a zinc oxide nanoparticle ink for printed electronics applications. *Flex. Print. Electron.* **2018**, *3*, 015001. [CrossRef]
60. Subramanian, V.; Bakhishev, T.; Redinger, D.; Volkman, S.K. Solution-processed zinc oxide transistors for low-cost electronics applications. *J. Disp. Technol.* **2009**, *5*, 525–530. [CrossRef]
61. Pimentel, A.; Fortunato, E.; Gonçalves, A.; Marques, A.; Águas, H.; Pereira, L.; Ferreira, I.; Martins, R. Polycrystalline intrinsic zinc oxide to be used in transparent electronic devices. *Thin Solid Film.* **2005**, *487*, 212–215. [CrossRef]
62. Faisal, S.; Jan, H.; Shah, S.A.; Shah, S.; Khan, A.; Akbar, M.T.; Rizwan, M.; Jan, F.; Wajidullah; Akhtar, N. Green synthesis of zinc oxide (ZnO) nanoparticles using aqueous fruit extracts of Myristica fragrans: Their characterizations and biological and environmental applications. *ACS Omega* **2021**, *6*, 9709–9722. [CrossRef]
63. Singh, T.A.; Das, J.; Sil, P.C. Zinc oxide nanoparticles: A comprehensive review on its synthesis, anticancer and drug delivery applications as well as health risks. *Adv. Colloid Interface Sci.* **2020**, *286*, 102317. [CrossRef]
64. Khuili, M.; Fazouan, N.; Abou El Makarim, H.; Atmani, E.; Rai, D.; Houmad, M. First-principles calculations of rare earth (RE = Tm, Yb, Ce) doped ZnO: Structural, optoelectronic, magnetic, and electrical properties. *Vacuum* **2020**, *181*, 109603. [CrossRef]
65. Kulandaisamy, A.J.; Elavalagan, V.; Shankar, P.; Mani, G.K.; Babu, K.J.; Rayappan, J.B.B. Nanostructured Cerium-doped ZnO thin film—A breath sensor. *Ceram. Int.* **2016**, *42*, 18289–18295. [CrossRef]
66. Zhang, Y.-H.; Peng, M.-X.; Yue, L.-J.; Chen, J.-L.; Gong, F.-L.; Xie, K.-F.; Fang, S.-M. A room-temperature aniline sensor based on Ce doped ZnO porous nanosheets with abundant oxygen vacancies. *J. Alloys Compd.* **2021**, *885*, 160988. [CrossRef]
67. Ren, X.; Gao, Y.; Zheng, L.; Wang, Z.; Wang, P.; Zheng, Z.; Liu, Y.; Cheng, H.; Dai, Y.; Huang, B. Oxygen vacancy enhancing CO_2 electrochemical reduction to CO on Ce-doped ZnO catalysts. *Surf. Interfaces* **2021**, *23*, 100923. [CrossRef]
68. Guan, H.; Mao, G.; Zhong, T.; Zhao, T.; Liang, S.; Xing, L.; Xue, X. A self-powered UV photodetector based on the hydrovoltaic and photoelectric coupling properties of ZnO nanowire arrays. *J. Alloys Compd.* **2021**, *867*, 159073. [CrossRef]
69. Zhou, X.; Zhang, Q.; Gan, L.; Li, X.; Li, H.; Zhang, Y.; Golberg, D.; Zhai, T. High—Performance solar-blind deep ultraviolet photodetector based on individual single-crystalline Zn_2GeO_4 nanowire. *Adv. Funct. Mater.* **2016**, *26*, 704–712. [CrossRef]
70. Liu, H.; Meng, J.; Zhang, X.; Chen, Y.; Yin, Z.; Wang, D.; Wang, Y.; You, J.; Gao, M.; Jin, P. High-performance deep ultraviolet photodetectors based on few-layer hexagonal boron nitride. *Nanoscale* **2018**, *10*, 5559–5565. [CrossRef] [PubMed]
71. Özgür, Ü.; Alivov, Y.I.; Liu, C.; Teke, A.; Reshchikov, M.A.; Doğan, S.; Avrutin, V.; Cho, S.-J.; Morkoç. A comprehensive review of ZnO materials and devices. *J. Appl. Phys.* **2005**, *98*, 041301. [CrossRef]
72. Faisal, M.; Ismail, A.A.; Ibrahim, A.A.; Bouzid, H.; Al-Sayari, S.A. Highly efficient photocatalyst based on Ce doped ZnO nanorods: Controllable synthesis and enhanced photocatalytic activity. *Chem. Eng. J.* **2013**, *229*, 225–233. [CrossRef]
73. Shkir, M.; Hakami, J.; Hossain, M.M.; Awwad, N.S.; Khan, A. Excellent photo-detection properties of cerium doped ZnO device fabricated by spray pyrolysis technique. *Inorg. Chem. Commun.* **2022**, *140*, 109439. [CrossRef]
74. Gupta, A.; Saurav, J.R.; Bhattacharya, S. Solar light based degradation of organic pollutants using ZnO nanobrushes for water filtration. *RSC Adv.* **2015**, *5*, 71472–71481. [CrossRef]
75. Sun, Q.; Li, K.; Wu, S.; Han, B.; Sui, L.; Dong, L. Remarkable improvement of TiO_2 for dye photocatalytic degradation by a facile post-treatment. *New J. Chem.* **2020**, *44*, 1942–1952. [CrossRef]
76. Rahman, Q.I.; Ahmad, M.; Misra, S.K.; Lohani, M. Effective photocatalytic degradation of rhodamine B dye by ZnO nanoparticles. *Mater. Lett.* **2013**, *91*, 170–174. [CrossRef]
77. Kumar, S.G.; Rao, K.K. Comparison of modification strategies towards enhanced charge carrier separation and photocatalytic degradation activity of metal oxide semiconductors (TiO_2, WO_3 and ZnO). *Appl. Surf. Sci.* **2017**, *391*, 124–148. [CrossRef]
78. Nemiwal, M.; Zhang, T.C.; Kumar, D. Recent progress in g-C_3N_4, TiO_2 and ZnO based photocatalysts for dye degradation: Strategies to improve photocatalytic activity. *Sci. Total Environ.* **2021**, *767*, 144896. [CrossRef] [PubMed]
79. Choudhary, S.; Sharma, M.; Krishnan, V.; Mohapatra, S. Facile synthesis of Ce doped ZnO nanowires for efficient photocatalytic removal of organic pollutants from water. *Mater. Today Commun.* **2023**, *34*, 105361. [CrossRef]

Disclaimer/Publisher's Note: The statements, opinions and data contained in all publications are solely those of the individual author(s) and contributor(s) and not of MDPI and/or the editor(s). MDPI and/or the editor(s) disclaim responsibility for any injury to people or property resulting from any ideas, methods, instructions or products referred to in the content.